Research Article

Nano Research
2022, 15(5): 3894–3900

ISSN 1998-0124 CN 11-5974/O4
https://doi.org/10.1007/s12274-021-4021-8

Plasmon-mediated photodecomposition of NH_3 via intramolecular charge transfer

Yimin Zhang[1,2,4], Weite Meng[2,3], Daqiang Chen[1,4], Lili Zhang[2], Shunfang Li[2] (✉), and Sheng Meng[1,4] (✉)

[1] *Beijing National Laboratory for Condensed Matter Physics and Institute of Physics, Chinese Academy of Sciences, Beijing 100190, China*
[2] *Key Laboratory of Material Physics, Ministry of Education, School of Physics and Microelectronics, Zhengzhou University, Zhengzhou 450001, China*
[3] *School of Chemical Engineering, Anhui University of Science and Technology, Huainan 232000, China*
[4] *School of Physical Sciences, University of Chinese Academy of Sciences, Beijing 100190, China*

Received: 22 September 2021 / **Revised:** 3 November 2021 / **Accepted:** 24 November 2021

ABSTRACT

As an excellent clean medium for hydrogen storage and fuel cell applications, the photolysis of ammonia via localized surface plasmon could be invoked as a promising route towards significantly reducing the temperature for conventional thermolysis. Here, we explore the underlying microscopic mechanism of ultrafast carrier dynamics in plasmon-mediated NH_3 photodecomposition at the single-molecular level using real-time time-dependent density functional theory. The NH_3 molecule adsorbed on the tip of archetypal magic metal clusters represented by tetrahedral Ag_{20} and icosahedral Ag_{147}, splits within a hundred femtoseconds upon laser pulse illumination. We found that the splitting of the first N-H bond is dominated by the intramolecular charge transfer driven by localized surface plasmon. Surprisingly, the phase of laser pulse could modulate the dynamics of charge transfer and thus affect the plasmon-induced bond breaking. These findings offer a new avenue for NH_3 decomposition and provide in-depth insights in designing highly efficient plasmon-mediated photocatalysts.

KEYWORDS

ammonia photodecomposition, localized surface plasmon, intramolecular charge transfer, time-dependent density functional theory

1 Introduction

Ammonia (NH_3), as an excellent medium for hydrogen storage/transport and fuel cell applications, can be liquefied easily at 20 °C at 0.8 MPa and contains a high percentage of hydrogen with a weight ratio of 17.8% [1–6]. The splitting of N-H bonds is crucial in the practical applications of NH_3 including hydrogen processing and transport in fuel cells [3, 7]. Previously, catalytic thermolysis of NH_3 has been widely investigated as a promising approach in the generation of hydrogen gas using a variety of metal particles (e.g., Fe, Ir, Ni, Ru, Pt) [3, 7–12], metal alloy [13, 14] and compounds [15] as catalysts. However, the conventional thermolysis of NH_3 usually requires overcoming the high reaction barriers at a relatively high temperature (~650 K) [1], which may significantly reduce the stability of catalysts and even thoroughly lose their activities due to nanoparticle sintering and aggregation [5, 6]. Nevertheless, the energy efficiency is also drastically reduced at high temperatures. Plasmon-mediated photodecomposition of NH_3 can be invoked to remedy the disadvantage of conventional thermolysis with the aid of plasmonic metal nanocatalysts, which enhance the light-matter interactions and facilitate the catalytic reactions thanks to the unique electronic and optical properties of plasmonic metal nanostructures.

Owing to their distinct properties such as extended lifetime, tunable resonance energy, ultrafast dynamics and enhanced optical absorption, localized surface plasmons (LSPs) in coinage metallic nanostructures (Au, Ag, Cu etc.) have sparked considerable attention in chemical and solar energy conversion, especially in photocatalysis [16–18]. Moreover, plasmon-driven photochemistry, as an efficient route to concentrate and channel the energy of solar energy into adsorbed molecules, has gained increasing attention thanks to its potential in drastically enhancing the energy conversion processes [19–30]. Most of the plasmon-induced chemical reactions are mainly dominated by either indirect carrier (electrons or holes) transfer or direct charge transfer mechanisms [20, 31–42], such as in the cases of H_2 activation [31–34], O_2 dissociation [17], and water splitting [38]. However, plasmon-mediated photodecomposition of NH_3, especially its underlying microscopic mechanism, has been seldom investigated. For examples, Zhou et al. [43] reported a plasmon-enhanced photodecomposition of ammonia using a ruthenium-doped Cu nanoparticles upon light illumination. In Zhou's work [43], although the role of hot carriers and thermal contributions in the dissociation process of NH_3 was explored, the underlying atomistic steps and microscopic mechanism such as the specific charge transfer pathway and its dynamics remain elusive. Very recently, Bao and co-workers [44] revealed that the plasmon excitation is able to facilitate ammonia decomposition by substantially reducing the effective reaction barriers on Cu_{10} clusters calculated by embedded correlated wavefunction theory. In the meantime, they predicted that the dominant reaction

Address correspondence to Shunfang Li, sflizzu@zzu.edu.cn; Sheng Meng, smeng@iphy.ac.cn

mechanism is the plasmon-induced resonant energy transfer, however, the microscopic dynamics of photocatalytic ammonia decomposition has not been illustrated.

Here, we investigate the underlying atomic steps and microscopic mechanisms of plasmon-enabled NH_3 photodissociation on plasmonic nanostructures represented by archetypal tetrahedral Ag_{20} (T_d-Ag_{20}) and icosahedral Ag_{147} (I_h-Ag_{147}) clusters at the single-molecular level and femtosecond timescale (Fig. 1(a)). By employing time-dependent density functional theory (TDDFT), we find that the intramolecular charge transfer dominates the photoreaction process, while the indirect or direct charge transfer mechanism is auxiliary via the ultrafast nonadiabatic molecular dynamics (NAMD) and carrier dynamics analysis. Furthermore, quite counterintuitively, besides the laser intensity, polarization, and photon energy, the carrier envelop phase of laser pulses can also modulate the specific charge transfer process and thus the N-H dissociation rate via tuning the occupation numbers of the excited states within the time regime of tens of femtoseconds. The above findings shed light on understanding the microscopic mechanism of NH_3 photodecomposition, and provide constructive insights for the design of highly efficient plasmon-mediated photocatalysts.

2 Results and discussion

2.1 Atomic configuration and absorption spectra

As a starting point, we first test the interaction of NH_3 molecule with T_d-Ag_{20} cluster with a few initial representative high symmetry adsorption configurations followed by geometry optimization. Owing to the broad range of absorption spectrum and excellent quality factor, silver is chosen here [45]. It is found that in the most stable structure the N atom in the C_{3v}-NH_3 species is close to the tip with the plane comprising the three H atoms perpendicular to the Ag-N axis (Fig. S1(a) in the Electronic Supplementary Material (ESM)). Second, to explore the response to light pulse, we present the absorption spectra of the T_d-Ag_{20} cluster, a freestanding NH_3 molecule, the optimized T_d-Ag_{20}-NH_3 complex, and the absorbed NH_3 component in the T_d-Ag_{20}-NH_3 complex, respectively, see Fig. 1(b). The first absorption peak of a freestanding NH_3 is located at 5.62 eV, corresponding to the transition from the highest occupied molecular orbitals (HOMO) and the lowest unoccupied molecular orbitals (LUMO). The Ag_{20}-NH_3 complex shows a visible blue shift of the major absorption peak to 4.72 eV relative to that of Ag_{20} (4.60 eV), indicating a non-negligible coupling between NH_3 and Ag_{20}. This can be also seen from the blue shift of the absorbed NH_3 relative to the freestanding NH_3.

2.2 Plasmon excitation

To investigate the response to laser illumination, the time-dependent N-H bond length in the adsorbed NH_3 on Ag_{20} under various maximum field strengths E_{max} are displayed in Fig. 1(c). Note that, here we only focus on the breaking of the first N-H bond, given that it is widely recognized as the rate-determining step possessing a higher activation barrier than that of breaking the other two N-H bonds [46, 47]. In addition, we assume that the threshold value of the bond length for N-H breaking is 2.0 Å, which is already considerably larger than the value (1.02 Å) of equilibrium N-H bond length in NH_3. From Fig. 1(c), one can see that the bond breaking accelerates with increasing E_{max}. Here, taking E_{max} = 0.7 V/Å and photon energy $\hbar\omega$ = 4.72 eV (Fig. S1(b) in the ESM) as a typical example, we detailed the process of the N-H breaking. The photon energy of 4.72 eV corresponds to the most evident plasmonic adsorption peak of the optimized T_d-Ag_{20}-NH_3 complex, as shown in Fig. 1(b) [48]. Specifically, one can see that, the N-H bond length initially exhibits a significant oscillation feature with a period of about 11 fs. Afterwards, the value of N-H bond length is gradually enlarged and the NH_3 molecule is split at 51 fs accompanied with a quick vanishing of the N-H bond oscillation. These findings imply that the NH_3 molecule is activated from the ground state to the vibrational excited state upon laser illumination.

As shown in Fig. 1(c), to elucidate the role of the Ag nanocluster, we have also compared the dynamic response of the NH_3 molecule to the laser pulse without the Ag nanostructure. Distinctly, the H-NH_2 distance of the freestanding NH_3 molecule maintains a stable oscillation at around 1.02 Å with a relatively small fluctuation amplitude rather than being split on T_d-Ag_{20} in the same laser field, indicating that the NH_3 splitting is driven by plasmonic excitation of Ag nanostructure. Particularly, as parameterized in Fig. S4 in the ESM, when increasing the photon energy ranging from 3.72 to 6.72 eV for a given pulse strength,

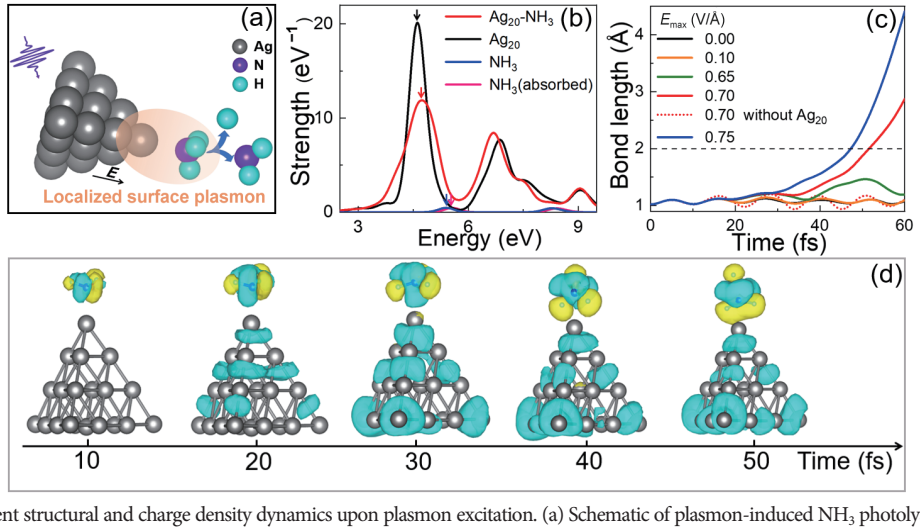

Figure 1 Time-dependent structural and charge density dynamics upon plasmon excitation. (a) Schematic of plasmon-induced NH_3 photolysis on T_d-Ag_{20} upon laser pulse. The black arrow shows the polarization direction of the laser. The area highlighted by light orange denotes the localized surface plasmon. (b) Absorption spectra of T_d-Ag_{20}-NH_3 complex, T_d-Ag_{20}, a freestanding NH_3 molecule and the absorbed NH_3 component in the T_d-Ag_{20}-NH_3 complex, respectively. (c) Ultrafast time-evolved H-NH_2 bond length under different E_{max}. The dashed line denotes the threshold of the bond breaking (2.0 Å). (d) Time-dependent charge density difference between the density at the present time and that at t = 0 under laser pulse, with an isosurface value of 0.03 Å^{-3}. Here, the blue and yellow denote the loss and gain of charge, respectively.

only as the photon energy equals the resonance energy of the adsorption peak (4.72 eV, see also Fig. 1(b)), can the N-H splitting be observed within 60 fs. These findings convincingly confirm that the NH_3 decomposition is indeed induced by plasmon excitation.

To present a direct view of the dissociation process, time-dependent structural and charge density evolution are investigated every 10 fs from t = 10 to 50 fs in Fig. 1(d). Here we define the time-dependent charge density differences (CDD) by $\Delta\rho(t) = \rho(t) - \rho(0)$, where $\rho(t)$ and $\rho(0)$ denote the charge density at the time t and at t = 0, respectively. During the splitting, the maximum bond length of N-H rises from 1.02 Å (t = 0) to 1.98 Å (t = 50 fs) accompanying with the bond oscillations, while the maximum bond angle of H-N-H increases from 107.4° to 135.1°. Moreover, according to the apparent evolution of charge density around the NH_3, we can find that the N atom loses charge while the three H atoms gain the charge, implying that there exists a strong intramolecular excitation within the NH_3 molecule. In the meantime, Ag nanocluster also loses some charges, suggesting additional charge transfer from the Ag_{20} to NH_3.

2.3 Time-dependent bond dynamics of Ag_{147}-NH_3 upon laser illumination

To explore the size effect on the NH_3 photolysis, we have also investigated the dynamic response of a NH_3 adsorbed on the tip (as shown in Figs. 2(a) and 2(b)) of Ag nanoclusters with different geometry and sizes, represented by an I_h-Ag_{147} with a diameter of 1.64 nm. The absorption spectra of I_h-Ag_{147}-NH_3 and I_h-Ag_{147} are shown in Fig. 2(c), where the absorption strength of Ag_{147} decreases upon the adsorption of NH_3, indicating that there exists a significant coupling between Ag_{147} and NH_3. However, as compared to the case of NH_3-Ag_{20}, the blue shift of adsorption peak from Ag_{147} to Ag_{147}-NH_3 was not readily observed, indicating that the coupling between I_h-Ag_{147} and NH_3 is weaker than that in T_d-Ag_{20}. Such findings can be rationalized by the relatively higher local electric field around the tip atom of the smaller T_d-Ag_{20}, which enhances the coupling of the polar molecule NH_3 with the Ag cluster. Furthermore, as shown in Fig. 2(d), the N-H bond length reaches 2.0 Å at t = 61.4 fs, demonstrating that plasmon-mediated photodecomposition rate of NH_3 can be also tuned by the size and shape effects.

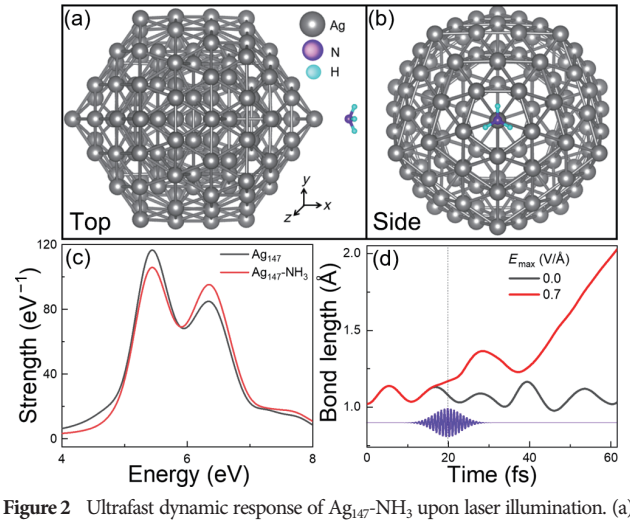

Figure 2 Ultrafast dynamic response of Ag_{147}-NH_3 upon laser illumination. (a) Top and (b) side view of the Ag_{147}-NH_3 system. (c) Absorption spectra of Ag_{147} and Ag_{147}-NH_3. Here, three characteristic absorption peaks are found at 3.63, 5.35, and 6.34 eV, respectively. (d) Time-dependent N-H bond length under the field strength E_{max} = 0.7 V/Å and photon energy $\hbar\omega$ = 5.35 eV. The inset (purple curve) represents the shape of laser pulse. The dashed line denotes that the field strength reaches the E_{max} = 0.7 V/Å at t = 20 fs.

2.4 Role of field enhancement and time-dependent excited-state charge density

To disclose the dominant mechanism for NH_3 photolysis, we first calculated the corresponding localized field enhancement (FE) factor [49] of Ag_{20}-NH_3, which is defined as

$$\mathrm{FE}(x) = \frac{[V_{\mathrm{eff}}(x+\delta x) - V_{\mathrm{eff}}(x)]}{e\delta x E_{\mathrm{ext}}} \quad (1)$$

where x, δx, v_{eff}, and E_{ext} are the position, mesh size along the polarized direction (x), effective potential, and external field strength, respectively. As shown in Fig. 3(a), an average FE of 1.4 is probed around the NH_3 species under an external field of E_{max} = 0.7 V/Å, which has a same magnitude with previous reports [50, 51]. However, even though a strong pulse of E_{max} = 1.0 V/Å (considering the FE of 1.4) is applied on a freestanding NH_3 molecule, the N-H bond length (black line) merely oscillates between 1.15–1.23 Å (Fig. 3(b)) rather than being split, excluding the purely field-driven mechanisms in plasmon-mediated photodecomposition of NH_3. Here, the temperature (heat) effect can be neglected due to the much longer time scale (~ 100 ps) than that in the present investigation (with a typical ultrafast timescale of ~ 60 fs) is needed to reach full thermal equilibrium [52, 53].

Now, we explore further the underlying mechanism of the plasmon-mediated photodecomposition of NH_3 adsorbed onto T_d-Ag_{20} nanocluster by analyzing the number of photoexcited electrons ΔQ in the adsorbed NH_3 molecule. As presented in Fig. 3(c), the ΔQ excited by a relatively low E_{max} (i.e., 0.10 V/Å) gradually increases to 0.25e upon laser illumination and tends to decay to 0e (E_{max}=0.00 V/Å) after the illumination. With the E_{max} increasing from 0.65, 0.70 to 0.75 V/Å, the calculated ΔQ rises to the maxima of 1.17, 1.31, and 1.39e respectively at around t = 20 fs, accompanied with a similar trend of oscillatory decay. These findings confirm the crucial roles of the excited-state charge transfer in plasmon-mediated photodecomposition of NH_3. We estimate that the plasmon-induced Ag-to-molecule charge transfer contributes ~25% of the total excited electrons in NH_3, as we detail below.

2.5 Time-dependent energy and occupation of Kohn-Sham (KS) states

To offer a comprehensive understanding of the photoexcited charge transfer, we analyze the time evolution of the occupation of the Kohn-Sham (KS) states shown in Fig. 4(a). For the sake of analysis, the weak laser pulse with a field strength of 0.1 V/Å is used. Similar results are observed under stronger laser pulses with the relative contribution of different excitation channels varies. Here, the occupation of KS states is calculated by projecting the time-dependent KS state onto the KS orbitals at time t = 0. Near the Fermi level, the occupations present a sloshing character, giving rise to the charge density oscillations around the Ag_{20} surface [54]. The excitation of electrons from the relatively low energy region to the high energy levels indicates the plasmon decay [55, 56]. The LPDOS (Fig. 4(b)) located on NH_3 are considerably broadened as compared to that in the gas phase, which further indicates the strong coupling of the NH_3 with T_d-Ag_{20}.

To further provide a straightforward description of the ultrafast carrier dynamics, the time-dependent occupation is presented in Fig. 4(c). It can be seen that the HOMO-2 (HOMO-5) has a contrary variation trend with LUMO+10 (LUMO+11), so does the trends between HOMO-3 (HOMO-4) and LUMO+12 (LUMO+13), which implies that there exists a charge transfer among these orbitals. Importantly, as shown in Fig. 4(d), we have

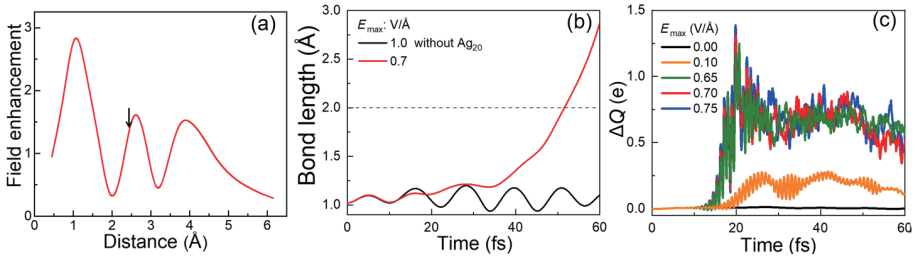

Figure 3 Field enhancement and excited carrier transfer. (a) Field enhancement effect in NH_3-T_d-Ag_{20}. The tip atom is located at the origin, and the black arrow denotes the location of the NH_3 molecule. (b) Time-dependent N-H bond lengths of freestanding NH_3 with E_{max} = 1.0 V/Å (black line) and NH_3-T_d-Ag_{20} with E_{max} = 0.7 V/Å (red line), respectively. (c) Number of photoexcited electrons ΔQ in the adsorbed NH_3 on T_d-Ag_{20} at different laser field strengths E_{max} ranging from 0 to 0.75 V/Å.

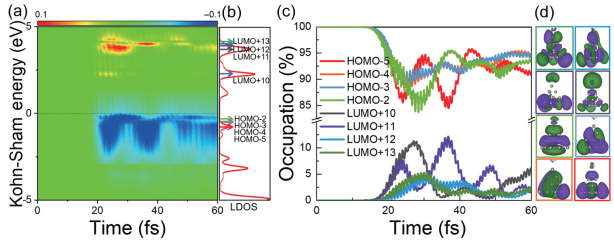

Figure 4 Time-dependent Kohn-Sham energy and occupations of NH_3-T_d-Ag_{20} system. (a) Time-dependent occupation of the KS states of the NH_3-T_d-Ag_{20} system with E_{max} = 0.1 V/Å. The dashed line denotes the Fermi level and the eight arrows from bottom to up denote eight KS states, i.e., HOMO-5, HOMO-4, HOMO-3, HOMO-2, LUMO+10, LUMO+11, LUMO+12, and LUMO+13, respectively. (b) Local projected density of states (LDOS) of NH_3 species at t = 0 fs. (c) Time-dependent occupation changes and (d) corresponding wavefunctions of the above eight states shown in different colors. Here, the isosurface value of the wavefunctions is 0.02 Å^{-3}.

also identified the dominant contributions of the involved orbitals, which is mainly determined by two factors, such as whether a coupling between the Ag nanoclusters and the NH_3 molecule exists and the strength of coupling.

To unravel the underlying charge transfer mechanism, the time-evolved transition coefficient of the above orbitals is specifically analyzed, as shown in Fig. 5(a), giving rise to a few interesting observations.

(i) The intramolecular charge transfer plays a dominant role. As shown in Fig. 5(a), one can see that significant electronic transition

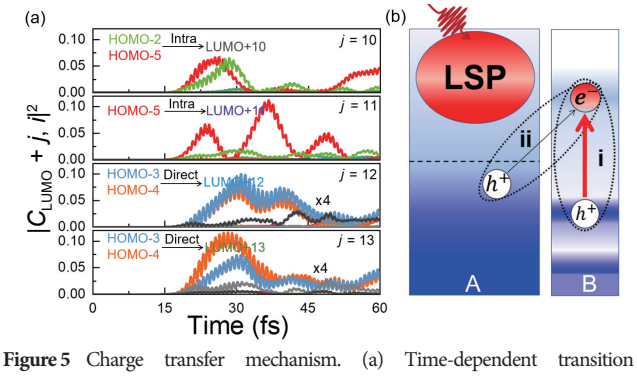

Figure 5 Charge transfer mechanism. (a) Time-dependent transition coefficient (squared) from all occupied states i to LUMO+10, LUMO+11, LUMO+12 and LUMO+13, respectively. The index i (i =1–14) denotes the numerical order of occupied states, while LUMO+j (j = 0–19) correspond to unoccupied states. A few representative orbitals making major contributions to density changes are labeled with corresponding colors in accordance with Fig. 4(c). (b) Schematic illustration of charge transfer mechanisms for plasmon-induced NH_3 photodecomposition. The red curve, red ellipse, black dashed line, and black arrows denote the laser pulse, localize surface plasmon (LSP), Fermi level, and the electron transfer, respectively. A: metal, B: adsorbate, i: intramolecular charge transfer, ii: direct charge transfer. The thickness of the black arrow denotes the relative contributions of the two mechanisms above.

is mainly originated from HOMO-i (i=2, 5) to LUMO+j (j=10, 11), which are all mainly contributed by the NH_3 component as illustrated in Fig. 4(d). Importantly, the energy gap of (LUMO+11)–(HOMO-5) ((LUMO+10)–(HOMO-2)) is 4.71 (4.50) eV, which is very close to the incident energy of the applied laser, suggesting that the charge transfer is a resonant process. Moreover, the dominant intramolecular charge transfer can be further confirmed by the similar analysis of time-evolved occupation and wavefunctions component for Ag_{147}-NH_3 (as shown in Figs. S3(a)–S3(c) and S4(a)–S4(c) in the ESM).

(ii) Auxiliary role of direct or indirect charge transfer from the Ag nanoparticle to NH_3. We also find that the direct charge transfer or indirect charge transfer plays an auxiliary role in the process of photodecomposition of NH_3. Such a hypothesis is also unambiguously confirmed by the time-dependent transition coefficient from all the occupied states HOMO-i to LUMO+j (j=12, 13) as shown in Fig. 5(a), demonstrating that the charge transfer is dominantly from the HOMO-3 and HOMO-4 states mainly located on Ag_{20} nanocluster, with an energy gap of 4.54 eV (close to the laser energy). Moreover, the overlap of the wavefunctions of Ag_{20} and NH_3 for LUMO+12 and LUMO+13 also offers auxiliary channels for plasmon decay and enables direct charge transfer from Ag_{20} to NH_3. As shown in Fig. 5(a), quantitatively, the direct charge transfer from Ag_{20} to NH_3 is about one fourth as compared to the intramolecular charge transfer, i.e., from HOMO-i (i=2, 5) to LUMO+j (j=10, 11). Note that, in contrast to the NH_3-T_d-Ag_{20}, the auxiliary role of direct charge transfer is replaced by an indirect charge transfer process in NH_3-I_h-Ag_{147} as shown in Figs. S3(a)–S3(c) and S4(d) in the ESM, which can be rationalized by the relatively weak coupling between the polar molecule NH_3 and the I_h-Ag_{147}.

To highlight the above mechanisms as revealed in present work, we summarize the charge transfer pathways schematically in Fig. 5(b). Upon laser illumination, the localized surface plasmon is generated in the Ag_{20}-NH_3 (Ag_{147}-NH_3) complex. The intramolecular charge transfer is resulted, which dominates the photolysis processes, while the direct/indirect nanoparticle-to-molecule charge transfer plays a secondary role. In particular, we note that the intramolecular charge transfer mechanism is proposed in Kazuma et al. [57], where they observed using scanning tunneling microscopy (STM) that an organic molecule (dimethyl disulfide [$(CH_3S)_2$]) splits on an Ag tip driven by plasmon excitation. However, the detailed ultrafast dynamics of excited carriers for the intramolecular charge transfer mechanism is missing. We report here that the plasmon-assisted intramolecular charge transfer mechanism also applies to the small inorganic molecule such as NH_3. Here, the reason why the auxiliary charge transfer mechanism is different in different nanocluster of sizes and geometries may be attributed to the strength of coupling between the nanocluster and the adsorbates, as well as the polarity of the adsorbates. Besides, the results may differ in other metal systems due to the difference in light absorption and plasmon intensity [24].

2.6 Modulation of laser pulse phase on the reaction rate

As shown in Figs. S5(a) and S5(b) in the ESM, the polarization direction can influence the bond length of N-H via modulating the number of photoexcited electrons upon the illumination of laser pulse. Except for the polarization direction, a surprising phenomenon is also observed (as shown in Fig. 6(a)) that the dissociation rate of NH_3 can be further tuned by the phase of laser pulses. Specifically, as shown in Fig. S6 in the ESM, the phase of laser leads to visible time-dependent differences when reaching the maximum strength, in both the amplitude and the exact time t for reaching maximum. Therefore, the phase of laser pulse can also serve as another degree of freedom to modulate the excited carrier transfer (as shown in Fig. 6(b) and Fig. S5(c) in the ESM). This phenomenon is also observed in other plasmon-mediated photocatalytic processes, such as in CO_2 splitting on T_d-Ag_{20} (as shown in Fig. 6(c)). Intuitively, the above results seem to be contrary to the conventional knowledge that the phase of laser neither change the energy injected into the system nor affect the subsequent reaction process such as the reaction rate. However, the present simulations at the single-molecule level reveals that, the plasmon-mediated photodecomposition processes may be very complex and can be further tuned by laser phases etc. within the time regime of 100 fs. This observation is expected to stimulate more elaborate theoretical and experimental investigations.

3 Conclusions

Employing the real-time time-dependent density functional theory, we have investigated the underlying microscopic mechanisms of plasmon-mediated NH_3 photodissociation on plasmonic materials represented by archetypal Ag nanoclusters of T_d-Ag_{20} and I_h-Ag_{147} at the single-molecular level. Via analyzing ultrafast structural and charge dynamics, we find that the intramolecular charge transfer dominates the photodissociation process of NH_3 on Ag nanoclusters, accompanied with a secondary direct or indirect charge transfer pathways. Surprisingly, we also find that the phase of laser pulse can be an important degree of freedom to modulate the photocatalytic reaction processes via tuning the specific occupations of the excited states and the subsequent charge transfer in the femtosecond time regime. Such observations are independent on the specific molecules as well as the sizes and shapes of plasmonic Ag nanoclusters. The present findings provide important insights on designing highly efficient plasmon-mediated photocatalysts, for instance for NH_3 conversion in practical hydrogen storage and fuel cells applications.

4 Methods

Most of the calculations are carried out using the TDDFT code OCTOPUS [58–60], and the home-built TDAP code [61–63] within local density approximation (LDA) for the exchange correlation functional. The simulation zone is defined by assigning a sphere around each atom with a radius of 6.0 Å and a spacing of 0.3 Å between grid points. Hartwigsen-Goedecker-Hutter pseudopotentials are used to represent the interactions between valence electrons and the atomic cores [64]. Nonadiabatic molecular dynamics is treated within the Ehrenfest scheme, where the ground state is used as the initial state. A time step of 0.002 fs is used in the calculations. An electromagnetic pulse (δ function) is used for the optical absorption spectrum. In the simulations, the NH_3 is initially placed 3.0 Å away from the tip of Ag_{20} and Ag_{147} as shown in Fig. S1(a) in the ESM and Figs. 2(a) and 2(b). The laser pulse is a Gaussian wave packet,

$$E(\omega,t) = E_{\max}\exp\left[-\frac{(t-t_0)^2}{2\tau^2}\right]\cos(\omega t-\omega t_0+\phi) \quad (2)$$

where the phase φ = 0, τ = 3.3 fs. The laser field reaches the maximum E_{max} at the time t_0 = 20 fs. We also examined laser pulse with different durations, which were demonstrated to result in the same trends.

Ground-state geometry structure optimizations are performed by DFT calculations as implemented in Vienna *Ab initio* simulation package (VASP). The interaction of valence electrons with atomic cores is described by the projector-augmented wave (PAW) method [65] as parameterized by the Perdew-Burke-Ernzerhof functional [66] with energy cutoff at 400 eV for the plane-wave basis set. The atomic structure of two systems positioned in a cubic supercell with the lattice constant of 30 Å, followed with full relaxation until the forces on each atom was less than 0.02 eV/Å and the convergence criterion for electronic step is 10^{-4} eV. Single Γ point is used for the structure optimizations.

Acknowledgements

We acknowledge financial support from MOST, the National Key Research and Development Project (No. 2021YFA1400200), the National Natural Science Foundation of China (NSFC) (Nos. 12025407, 11774396, 91850120, 11934003, and 11674289), and CAS (XDB330301).

Notes

The authors declare no competing interests.

Electronic Supplementary Material: Supplementary material (further details of atomic geometries, laser pulse and time-evolved bond length at different photon energy, polarization, and laser phase for Ag_{20}-NH_3, time-evolved occupations for Ag_{147}-NH_3, applied laser intensity) is available in the online version of this article at https://doi.org/10.1007/s12274-021-4021-8.

References

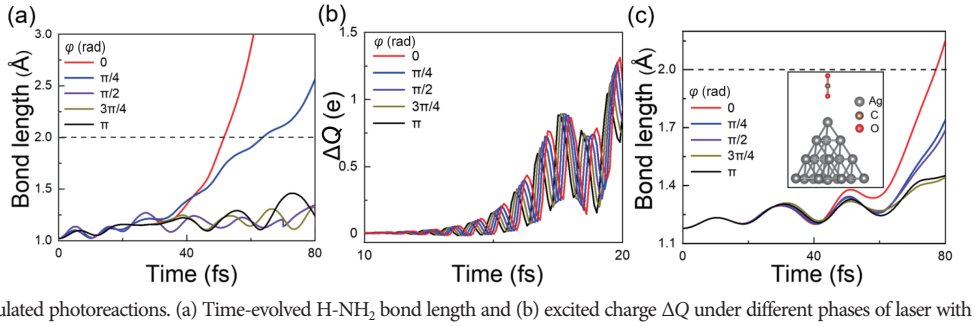

Figure 6 Phase-modulated photoreactions. (a) Time-evolved H-NH_2 bond length and (b) excited charge ΔQ under different phases of laser with fixed E_{max} = 0.7 V/Å and $\hbar\omega$ = 4.72 eV. The dashed line denotes the bond breaking. (c) Time-evolved C-O bond length under different phase of laser with fixed E_{max} = 2.5 V/Å and $\hbar\omega$ = 4.56 eV. The inset denotes the configuration of CO_2-T_d-Ag_{20}.

[1] Schüth, F.; Palkovits, R.; Schlögl, R.; Su, D. S. Ammonia as a possible element in an energy infrastructure: Catalysts for ammonia decomposition. *Energy Environ. Sci.* **2012**, *5*, 6278–6289.
[2] Lamb, K. E.; Dolan, M. D.; Kennedy, D. F. Ammonia for hydrogen storage: A review of catalytic ammonia decomposition and hydrogen separation and purification. *Int. J. Hydrogen Energy* **2019**, *44*, 3580–3593.
[3] Guo, J. P.; Chen, P. Catalyst: NH_3 as an energy carrier. *Chem* **2017**, *3*, 709–712.
[4] Wu, H.; Cheng, Y. J.; Fan, Y. P.; Lu, X. M.; Li, L. X.; Liu, B. Z.; Li, B. J.; Lu, S. Y. Metal-catalyzed hydrolysis of ammonia borane: Mechanism, catalysts, and challenges. *Int. J. Hydrogen Energy* **2020**, *45*, 30325–30340.
[5] Wu, H.; Cheng, Y. J.; Wang, B. Y.; Wang, Y.; Wu, M.; Li, W. D.; Liu, B. Z.; Lu, S. Y. Carbon dots-confined CoP-CoO nanoheterostructure with strong interfacial synergy triggered the robust hydrogen evolution from ammonia borane. *J. Energy Chem.* **2021**, *57*, 198–205.
[6] Wu, H.; Wu, M.; Wang, B. Y.; Yong, X.; Liu, Y. S.; Li, B. J.; Liu, B. Z.; Lu, S. Y. Interface electron collaborative migration of Co-Co_3O_4/carbon dots: Boosting the hydrolytic dehydrogenation of ammonia borane. *J. Energy Chem.* **2020**, *48*, 43–53.
[7] Wang, Z. Q.; Cai, Z. F.; Wei, Z. Highly active ruthenium catalyst supported on barium hexaaluminate for ammonia decomposition to CO_x-free hydrogen. *ACS Sustainable Chem. Eng.* **2019**, *7*, 8226–8235.
[8] Tsai, W.; Vajo, J. J.; Weinberg, W. H. Inhibition by hydrogen of the heterogeneous decomposition of ammonia on platinum. *J. Phys. Chem.* **1985**, *89*, 4926–4932.
[9] Tsai, W.; Weinberg, W. H. Steady-state decomposition of ammonia on the ruthenium(001) surface. *J. Phys. Chem.* **1987**, *91*, 5302–5307.
[10] Wang, L.; Yi, Y. H.; Zhao, Y.; Zhang, R.; Zhang, J. L.; Guo, H. C. NH_3 decomposition for H_2 generation: Effects of cheap metals and supports on plasma-catalyst synergy. *ACS Catal.* **2015**, *5*, 4167–4174.
[11] Hayashi, F.; Toda, Y.; Kanie, Y.; Kitano, M.; Inoue, Y.; Yokoyama, T.; Hara, M.; Hosono, H. Ammonia decomposition by ruthenium nanoparticles loaded on inorganic electride $C_{12}A_7$: e^-. *Chem. Sci.* **2013**, *4*, 3124–3130.
[12] Yeo, S. C.; Han, S. S.; Lee, H. M. Mechanistic investigation of the catalytic decomposition of ammonia (NH_3) on an Fe(100) surface: A DFT study. *J. Phys. Chem. C* **2014**, *118*, 5309–5316.
[13] Guo, W.; Vlachos, D. G. Patched bimetallic surfaces are active catalysts for ammonia decomposition. *Nat. Commun.* **2015**, *6*, 8619.
[14] Hansgen, D. A.; Vlachos, D. G.; Chen, J. G. Using first principles to predict bimetallic catalysts for the ammonia decomposition reaction. *Nat. Chem.* **2010**, *2*, 484–489.
[15] Zheng, W. Q.; Cotter, T. P.; Kaghazchi, P.; Jacob, T.; Frank, B.; Schlichte, K.; Zhang, W.; Su, D. S.; Schüth, F.; Schlögl, R. Experimental and theoretical investigation of molybdenum carbide and nitride as catalysts for ammonia decomposition. *J. Am. Chem. Soc.* **2013**, *135*, 3458–3464.
[16] Nie, S. M.; Emory, S. R. Probing single molecules and single nanoparticles by surface-enhanced Raman scattering. *Science* **1997**, *275*, 1102–1106.
[17] Prodan, E.; Radloff, C.; Halas, N. J.; Nordlander, P. A hybridization model for the plasmon response of complex nanostructures. *Science* **2003**, *302*, 419–422.
[18] Xu, H. X.; Bjerneld, E. J.; Käll, M.; Börjesson, L. Spectroscopy of single hemoglobin molecules by surface enhanced Raman scattering. *Phys. Rev. Lett.* **1999**, *83*, 4357–4360.
[19] Robatjazi, H.; Bahauddin, S. M.; Doiron, C.; Thomann, I. Direct plasmon-driven photoelectrocatalysis. *Nano Lett.* **2015**, *15*, 6155–6161.
[20] Christopher, P.; Xin, H. L.; Linic, S. Visible-light-enhanced catalytic oxidation reactions on plasmonic silver nanostructures. *Nat. Chem.* **2011**, *3*, 467–472.
[21] Linic, S.; Christopher, P.; Ingram, D. B. Plasmonic-metal nanostructures for efficient conversion of solar to chemical energy. *Nat. Mater.* **2011**, *10*, 911–921.
[22] Linic, S.; Christopher, P.; Xin, H. L.; Marimuthu, A. Catalytic and photocatalytic transformations on metal nanoparticles with targeted geometric and plasmonic properties. *Acc. Chem. Res.* **2013**, *46*, 1890–1899.
[23] Swearer, D. F.; Zhao, H. Q.; Zhou, L. N.; Zhang, C.; Robatjazi, H.; Martirez, J. M. P.; Krauter, C. M.; Yazdi, S.; McClain, M. J.; Ringe, E. et al. Heterometallic antenna-reactor complexes for photocatalysis. *Proc. Natl. Acad. Sci. USA* **2016**, *113*, 8916–8920.
[24] Hartland, G. V. Optical studies of dynamics in noble metal nanostructures. *Chem. Rev.* **2011**, *111*, 3858–3887.
[25] Giannini, V.; Fernández-Domínguez, A. I.; Heck, S. C.; Maier, S. A. Plasmonic nanoantennas: Fundamentals and their use in controlling the radiative properties of nanoemitters. *Chem. Rev.* **2011**, *111*, 3888–3912.
[26] Yang, H.; Wang, Z. H.; Zheng, Y. Y.; He, L. Q.; Zhan, C.; Lu, X. H.; Tian, Z. Q.; Fang, P. P.; Tong, Y. X. Tunable wavelength enhanced photoelectrochemical cells from surface plasmon resonance. *J. Am. Chem. Soc.* **2016**, *138*, 16204–16207.
[27] Sprague-Klein, E. A.; Negru, B.; Madison, L. R.; Coste, S. C.; Rugg, B. K.; Felts, A. M.; McAnally, M. O.; Banik, M.; Apkarian, V. A.; Wasielewski, M. R. et al. Photoinduced plasmon-driven chemistry in trans-1, 2-bis(4-pyridyl)ethylene gold nanosphere oligomers. *J. Am. Chem. Soc.* **2018**, *140*, 10583–10592.
[28] Zhang, H. W.; Itoi, T.; Konishi, T.; Izumi, Y. Dual photocatalytic roles of light: Charge separation at the band gap and heat via localized surface plasmon resonance to convert CO_2 into CO over silver-zirconium oxide. *J. Am. Chem. Soc.* **2019**, *141*, 6292–6301.
[29] Hu, C. Y.; Chen, X.; Jin, J. B.; Han, Y.; Chen, S. M.; Ju, H. X.; Cai, J.; Qiu, Y. R.; Gao, C.; Wang, C. M. et al. Surface plasmon enabling nitrogen fixation in pure water through a dissociative mechanism under mild conditions. *J. Am. Chem. Soc.* **2019**, *141*, 7807–7814.
[30] Rao, V. G.; Aslam, U.; Linic, S. Chemical requirement for extracting energetic charge carriers from plasmonic metal nanoparticles to perform electron-transfer reactions. *J. Am. Chem. Soc.* **2019**, *141*, 643–647.
[31] Brongersma, M. L.; Halas, N. J.; Nordlander, P. Plasmon-induced hot carrier science and technology. *Nat. Nanotechnol.* **2015**, *10*, 25–34.
[32] Linic, S.; Aslam, U.; Boerigter, C.; Morabito, M. Photochemical transformations on plasmonic metal nanoparticles. *Nat. Mater.* **2015**, *14*, 567–576.
[33] Thrall, E. S.; Steinberg, A. P.; Wu, X. M.; Brus, L. E. The role of photon energy and semiconductor substrate in the plasmon-mediated photooxidation of citrate by silver nanoparticles. *J. Phys. Chem. C* **2013**, *117*, 26238–26247.
[34] Mukherjee, S.; Libisch, F.; Large, N.; Neumann, O.; Brown, L. V.; Cheng, J.; Lassiter, J. B.; Carter, E. A.; Nordlander, P.; Halas, N. J. Hot electrons do the impossible: Plasmon-induced dissociation of H_2 on Au. *Nano Lett.* **2013**, *13*, 240–247.
[35] Mukherjee, S.; Zhou, L. N.; Goodman, A. M.; Large, N.; Ayala-Orozco, C.; Zhang, Y.; Nordlander, P.; Halas, N. J. Hot-electron-induced dissociation of H_2 on gold nanoparticles supported on SiO_2. *J. Am. Chem. Soc.* **2014**, *136*, 64–67.
[36] Zhang, Y.; Nelson, T.; Tretiak, S.; Guo, H.; Schatz, G. C. Plasmonic hot-carrier-mediated tunable photochemical reactions. *ACS Nano* **2018**, *12*, 8415–8422.
[37] Yan, L.; Ding, Z. J.; Song, P.; Wang, F. W.; Meng, S. Plasmon-induced dynamics of H_2 splitting on a silver atomic chain. *Appl. Phys. Lett.* **2015**, *107*, 083102.
[38] Yan, L.; Wang, F. W.; Meng, S. Quantum mode selectivity of plasmon-induced water splitting on gold nanoparticles. *ACS Nano* **2016**, *10*, 5452–5458.
[39] Yan, J.; Jacobsen, K. W.; Thygesen, K. S. First-principles study of surface plasmons on Ag(111) and H/Ag(111). *Phys. Rev. B* **2011**, *84*, 235430.
[40] Kale, M. J.; Avanesian, T.; Xin, H. L.; Yan, J.; Christopher, P. Controlling catalytic selectivity on metal nanoparticles by direct photoexcitation of adsorbate-metal bonds. *Nano Lett.* **2014**, *14*, 5405–5412.
[41] Kale, M. J.; Avanesian, T.; Christopher, P. Direct photocatalysis by plasmonic nanostructures. *ACS Catal.* **2014**, *4*, 116–128.
[42] Kumar, P. V.; Rossi, T. P.; Marti-Dafcik, D.; Reichmuth, D.; Kuisma, M.; Erhart, P.; Puska, M. J.; Norris, D. J. Plasmon-induced direct hot-

carrier transfer at metal-acceptor interfaces. *ACS Nano* **2019**, *13*, 3188–3195.

[43] Zhou, L.; Swearer, D. F.; Zhang, C.; Robatjazi, H.; Zhao, H. Q.; Henderson, L.; Dong, L. L.; Christopher, P.; Carter, E. A.; Nordlander, P. et al. Quantifying hot carrier and thermal contributions in plasmonic photocatalysis. *Science* **2018**, *362*, 69–72.

[44] Bao, J. L.; Carter, E. A. Surface-plasmon-induced ammonia decomposition on copper: Excited-state reaction pathways revealed by embedded correlated wavefunction theory. *ACS Nano* **2019**, *13*, 9944–9957.

[45] Rycenga, M.; Cobley, C. M.; Zeng, J.; Li, W. Y.; Moran, C. H.; Zhang, Q.; Qin, D.; Xia, Y. N. Controlling the synthesis and assembly of silver nanostructures for plasmonic applications. *Chem. Rev.* **2011**, *111*, 3669–3712.

[46] Bradford, M. C. J.; Fanning, P. E.; Vannice, M. A. Kinetics of NH_3 decomposition over well dispersed Ru. *J. Catal.* **1997**, *172*, 479–484.

[47] Ganley, J. C.; Thomas, F.; Seebauer, E. G.; Masel, R. I. A priori catalytic activity correlations: The difficult case of hydrogen production from ammonia. *Catal. Lett.* **2004**, *96*, 117–122.

[48] Aikens, C. M.; Li, S. Z.; Schatz, G. C. From discrete electronic states to plasmons: TDDFT optical absorption properties of Ag_n(n= 10, 20, 35, 56, 84, 120) tetrahedral clusters. *J. Phys. Chem. C* **2008**, *112*, 11272–11279.

[49] Song, P.; Nordlander, P.; Gao, S. W. Quantum mechanical study of the coupling of plasmon excitations to atomic-scale electron transport. *J. Chem. Phys.* **2011**, *134*, 074701.

[50] Yan, L.; Xu, J. Y.; Wang, F. W.; Meng, S. Plasmon-induced ultrafast hydrogen production in liquid water. *J. Phys. Chem. Lett.* **2018**, *9*, 63–69.

[51] Awazu, K.; Fujimaki, M.; Rockstuhl, C.; Tominaga, J.; Murakami, H.; Ohki, Y.; Yoshida, N.; Watanabe, T. A plasmonic photocatalyst consisting of silver nanoparticles embedded in titanium dioxide. *J. Am. Chem. Soc.* **2008**, *130*, 1676–1680.

[52] Adleman, J. R.; Boyd, D. A.; Goodwin, D. G.; Psaltis, D. Heterogenous catalysis mediated by plasmon heating. *Nano Lett.* **2009**, *9*, 4417–4423.

[53] Golubev, A. A.; Khlebtsov, B. N.; Rodriguez, R. D.; Chen, Y.; Zahn, D. R. T. Plasmonic heating plays a dominant role in the plasmon-induced photocatalytic reduction of 4-nitrobenzenethiol. *J. Phys. Chem. C* **2018**, *122*, 5657–5663.

[54] Townsend, E.; Bryant, G. W. Plasmonic properties of metallic nanoparticles: The effects of size quantization. *Nano Lett.* **2012**, *12*, 429–434.

[55] Townsend, E.; Bryant, G. W. Which resonances in small metallic nanoparticles are plasmonic? *J. Opt.* **2014**, *16*, 114022.

[56] Ma, J.; Wang, Z.; Wang, L. W. Interplay between plasmon and single-particle excitations in a metal nanocluster. *Nat. Commun.* **2015**, *6*, 10107.

[57] Kazuma, E.; Jung, J.; Ueba, H.; Trenary, M.; Kim, Y. Real-space and real-time observation of a plasmon-induced chemical reaction of a single molecule. *Science* **2018**, *360*, 521–526.

[58] Castro, A.; Appel, H.; Oliveira, M.; Rozzi, C. A.; Andrade, X.; Lorenzen, F.; Marques, M. A. L.; Gross, E. K. U.; Rubio, A. Octopus: A tool for the application of time-dependent density functional theory. *Phys. Status Solidi (B)* **2006**, *243*, 2465–2488.

[59] Andrade, X.; Alberdi-Rodriguez, J.; Strubbe, D. A.; Oliveira, M. J. T.; Nogueira, F.; Castro, A.; Muguerza, J.; Arruabarrena, A.; Louie, S. G.; Aspuru-Guzik, A. et al. Time-dependent density-functional theory in massively parallel computer architectures: The OCTOPUS project. *J. Phys. :Condens. Matter* **2012**, *24*, 233202.

[60] Andrade, X.; Strubbe, D.; De Giovannini, U.; Larsen, A. H.; Oliveira, M. J. T.; Alberdi-Rodriguez, J.; Varas, A.; Theophilou, I.; Helbig, N.; Verstraete, M. J. et al. Real-space grids and the octopus code as tools for the development of new simulation approaches for electronic systems. *Phys. Chem. Chem. Phys.* **2015**, *17*, 31371–31396.

[61] Meng, S.; Kaxiras, E. Real-time, local basis-set implementation of time-dependent density functional theory for excited state dynamics simulations. *J. Chem. Phys.* **2008**, *129*, 054110.

[62] Ma, W.; Zhang, J.; Yan, L.; Jiao, Y.; Gao, Y.; Meng, S. Recent progresses in real-time local-basis implementation of time dependent density functional theory for electron-nucleus dynamics. *Comput. Mater. Sci.* **2016**, *112*, 478–486.

[63] Lian, C.; Guan, M. X.; Hu, S. Q.; Zhang, J.; Meng, S. Photoexcitation in solids: First-principles quantum simulations by real-time TDDFT (Adv. Theory Simul. 8/2018). *Adv. Theory Simul.* **2018**, *1*, 1870018.

[64] Troullier, N.; Martins, J. L. Efficient pseudopotentials for plane-wave calculations. *Phys. Rev. B* **1991**, *43*, 1993–2006.

[65] Yabana, K.; Bertsch, G. F. Time-dependent local-density approximation in real time. *Phys. Rev. B* **1996**, *54*, 4484–4487.

[66] Perdew, J. P.; Burke, K.; Ernzerhof, M. Generalized gradient approximation made simple. *Phys. Rev. Lett.* **1996**, *77*, 3865–3868.